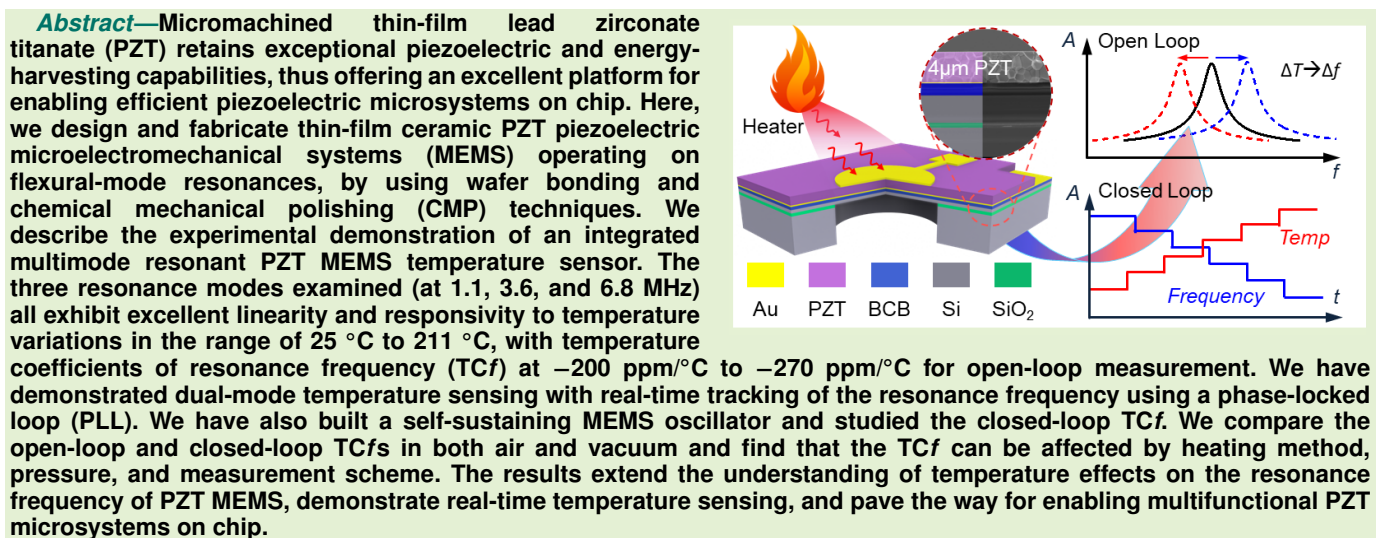


# Micromachined Thin Film Ceramic PZT Multimode Resonant Temperature Sensor

Wen Sui<sup>ID</sup>, Graduate Student Member, IEEE, Tahmid Kaisar<sup>ID</sup>, Graduate Student Member, IEEE, Haoran Wang<sup>ID</sup>, Yihao Wu<sup>ID</sup>, Graduate Student Member, IEEE, Jaesung Lee<sup>ID</sup>, Member, IEEE, Huikai Xie<sup>ID</sup>, Fellow, IEEE, and Philip X.-L. Feng<sup>ID</sup>, Senior Member, IEEE



**Index Terms**—Ceramic lead zirconate titanate (PZT), microelectromechanical systems (MEMS), oscillator, phase-locked loop (PLL), temperature sensor.

Manuscript received 1 February 2023; revised 17 March 2023 and 23 April 2023; accepted 26 April 2023. Date of publication 14 July 2023; date of current version 14 March 2024. This work was supported in part by the National Institutes of Health (NIH) under Award R01EB020601; in part by the National Science Foundation (NSF) Division of Electrical, Communications and Cyber Systems (ECCS) Early-Concept Grants for Exploratory Research (EAGER) Program under Grant 2221881; and in part by the Finish Line Award from the Graduate School, University of Florida. This research was conducted at the University of Florida (UF), with contributions from authors when they were affiliated with UF. The associate editor coordinating the review of this article and approving it for publication was Prof. Jeong Bong Lee. (*Wen Sui and Tahmid Kaisar contributed equally to this work.*) (*Corresponding author: Philip X.-L. Feng.*)

Wen Sui, Tahmid Kaisar, Yihao Wu, Jaesung Lee, and Philip X.-L. Feng are with the Department of Electrical and Computer Engineering, Herbert Wertheim College of Engineering, University of Florida, Gainesville, FL 32611 USA (e-mail: wen.sui@ufl.edu; kaisart@ufl.edu; philip.feng@ufl.edu).

Haoran Wang was with the Department of Electrical and Computer Engineering, Herbert Wertheim College of Engineering, University of Florida, Gainesville, FL 32611 USA. He is now with Applied Materials Inc., Sunnyvale, CA 94086 USA.

Huikai Xie was with the Department of Electrical and Computer Engineering, Herbert Wertheim College of Engineering, University of Florida, Gainesville, FL 32611 USA.

Digital Object Identifier 10.1109/JSEN.2023.3294125

## I. INTRODUCTION

TOWARDS emerging industry 4.0 with prevailing Internet of Things (IoT) and the swarm of trillion sensors perspective, new advances in miniaturized, ultralow-power, or self-powering, multifunctional integrated sensors are increasingly demanded [1], [2]. Miniature temperature sensors, in particular, while being ubiquitous and having various existing solutions in conventional methods (e.g., thermistors, diodes, and transistors), still face new challenges in emerging applications, such as in smart buildings and industry plants, self-driving vehicles (e.g., monitoring the temperature of engine or other critical parts), fire-fighting drones, and medical implants [3], [4]. High precision, energy efficiency, and harsh-environment resilience are essential in such scenarios while conventional thermistor/diode options are increasingly insufficient or unfit. Harsh environments are not only limited to space and areas affected by natural hazards [5], [6]. There are also various industrial applications which impose harsh conditions on devices. Jet engines or downhole gas and oil industry, for instance, subject monitoring devices to high temperatures and pressures [7]. There is a high demand for passive wireless temperature sensing in various applications,

especially inaccessible locations, and hazardous environments, where long lifetime is essential, or harsh environments, where battery lifetime can be severely shortened [8].

Resonant sensors have a frequency as output and have become a powerful solution to sensing many physical parameters, such as mass, pressure, temperature, and viscosity. Remote temperature sensors were demonstrated in 1987 based on lithium niobate ( $\text{LiNbO}_3$ ) surface acoustic wave (SAW) resonators [9]. A plethora of devices have recently been developed and are currently in widespread use [10]. Resonant temperature sensors have often been fabricated using piezoelectric crystals, such as  $\text{LiNbO}_3$  or quartz. The high responsivity to temperature in particular cuts of quartz crystals has made it possible to manufacture sensors with very high resolution ( $0.001\text{ }^\circ\text{C}$ ) [11]. Despite this feature, the main disadvantages of these sensors are their relatively large sizes and the incompatibility of their fabrication processes with mainstream silicon microfabrication and scalable manufacturing technologies [12]. Microelectromechanical systems (MEMS) technology has witnessed tremendous development over recent decades. MEMS devices are sensitive to external perturbations, making them excellent candidates for physical sensors, particularly resonant-mode sensors for physical stimuli and perturbations, such as pressure, vibration, humidity, mass, and temperature [13], [14], [15].

Regarding MEMS resonators for temperature sensing applications, it is essential to investigate the temperature effects on the resonance frequency, and a large absolute value of the temperature coefficient of resonance frequency ( $\text{TC}_f$ ) is preferred. Up to date,  $\text{TC}_f$  values ( $\text{TC}_f$ s hereafter for simplicity) of MEMS with diverse structures based on various materials [Si, AlN, gallium nitride (GaN), and silicon carbide (SiC)] have been extensively reported [16], [17], [18], [19], [20]. However, the majority of research has concentrated on achieving near-zero  $\text{TC}_f$  through improving the structural design, doping, and stress regulation, so as to enable MEMS for timing references [21], [22], [23], [24], [25]. Most  $\text{TC}_f$ s reported in literatures are less than  $100\text{ ppm}/\text{ }^\circ\text{C}$ . Only a few studies are dedicated to obtaining large  $\text{TC}_f$ s, which are required for temperature sensing applications [26], [27]. On the other hand, three-dimensional (3-D) integration and packaging of MEMS with integrated circuits (ICs) is an emerging technology that could lead to a new paradigm of future highly integrated microsystems, enabling multifunctionality, high performance, small size and low weight, and at low cost [28]. It would be interesting if we had MEMS energy harvesting, MEMS temperature sensor, and ICs all on one silicon die.

Micromachined thin-film lead zirconate titanate (PZT) retains exceptional piezoelectric and energy-harvesting capabilities, which is an excellent platform for enabling efficient piezoelectric microsystems on-chip [29], [30], [31]. PZT piezoelectric micromachined ultrasonic transducers (pMUT) are a versatile technology for ultrasonic sensing and photoacoustic imaging [32], [33]. It would be appealing to have a PZT MEMS temperature sensor which can be self-powered and integrated into PZT pMUT arrays for continuous monitoring and sensing in ordinary and harsh environments. A vision of future 3-D integration of PZT MEMS with ICs is illustrated in Fig. 1(a). In terms of fabrication, sputtered PZT or sol-gel PZT films are commonly limited by high processing temperature, high stress, low deposition rate, and small thickness [34], [35]. Ceramic PZT materials with a wide

range of thickness, on the other hand, can effectively boost the piezoelectric response and reduce the processing temperature [29], [36]. However, its fragileness makes it challenging to thin the ceramic PZT down to sub- $10\text{ }\mu\text{m}$  thickness.

In this work, we design and fabricate thin-film ceramic PZT piezoelectric MEMS transducers operating on flexural-mode resonances by using wafer bonding and chemical mechanical polishing (CMP) techniques. We thoroughly investigate the effect of temperature on the resonance of PZT MEMS under different conditions using various heating techniques, pressures, and measurement approaches. We have demonstrated temperature sensing with real-time tracking of the resonance frequency using a phase-locked loop (PLL) and by building a self-sustaining MEMS oscillator.

## II. DESIGN OF EXPERIMENT

### A. Structural Design of PZT MEMS

The multimode resonance frequency of a circular diaphragm resonator can be expressed as follows [37]:

$$f_n = \left( \frac{k_n r}{2\pi} \right) \sqrt{\frac{D}{\rho t r^4} \left[ (k_n r)^2 + \frac{\gamma r^2}{D} \right]} \quad (1)$$

where  $n$  represents the mode number,  $r$  is the radius,  $(k_n r)^2$  is a numerically calculated modal parameter [ $(k_0 r)^2 = 10.215$ ,  $(k_1 r)^2 = 21.260$ ,  $(k_2 r)^2 = 34.877$ , and  $(k_3 r)^2 = 39.771$ ],  $\rho$  denotes the volume mass density,  $t$  is the thickness,  $\gamma$  refers to the built-in tension (in [ $\text{N/m}$ ], or stress [ $\text{N/m}^2$  or  $\text{Pa}$ ] times thickness), and  $D$  is the flexural rigidity,  $D = E_Y t^3/[12(1 - \nu^2)]$  in which  $E_Y$  and  $\nu$  are Young's modulus and Poisson's ratio, respectively. Equation (1) yields a mixed elasticity model, in which both flexural rigidity (dominated by the thickness and elastic modulus) and built-in tension (stress) play key roles in determining the resonance frequency. As  $\gamma r^2/D$  goes very small and negligible in (1), flexural rigidity  $D$  dominates the frequency, and the model approaches the plate limit

$$f_n = \frac{(k_n r)^2}{2\pi r^2} \sqrt{\frac{D}{\rho t}}. \quad (2)$$

For a circular plate with multilayers, as illustrated in Fig. 2, the effective flexural rigidity and mass density can be expressed as follows:

$$D = \sum_i \left( \frac{E_{Yi}}{1 - \nu_i^2} \right) \left( \frac{t_i^3}{12} + d_i^2 t_i \right) \quad (3)$$

$$\rho = \sum_i \left( \rho_i \frac{t_i}{t} \right). \quad (4)$$

Here,  $E_{Yi}$ ,  $\nu_i$ ,  $t_i$ , and  $\rho_i$  are Young's modulus, Poisson's ratio, thickness, and volume mass density of the  $i$ th layer, respectively, and  $d_i$  is the distance between the midplane of the  $i$ th layer to the neutral plane. By controlling the thickness of each layer, the neutral plane is set within the benzocyclobutene (BCB) layer (Fig. 2), as indicated by

$$Z_n = \frac{\sum_{i=1}^m \frac{E_{Yi} Z_i t_i}{1 - \nu_i^2}}{\sum_{i=1}^m \frac{E_{Yi} t_i}{1 - \nu_i^2}} \quad (5)$$

where  $Z_n$  defines the distance from the neutral plane to the reference plane, and  $Z_i$  is the distance from the reference

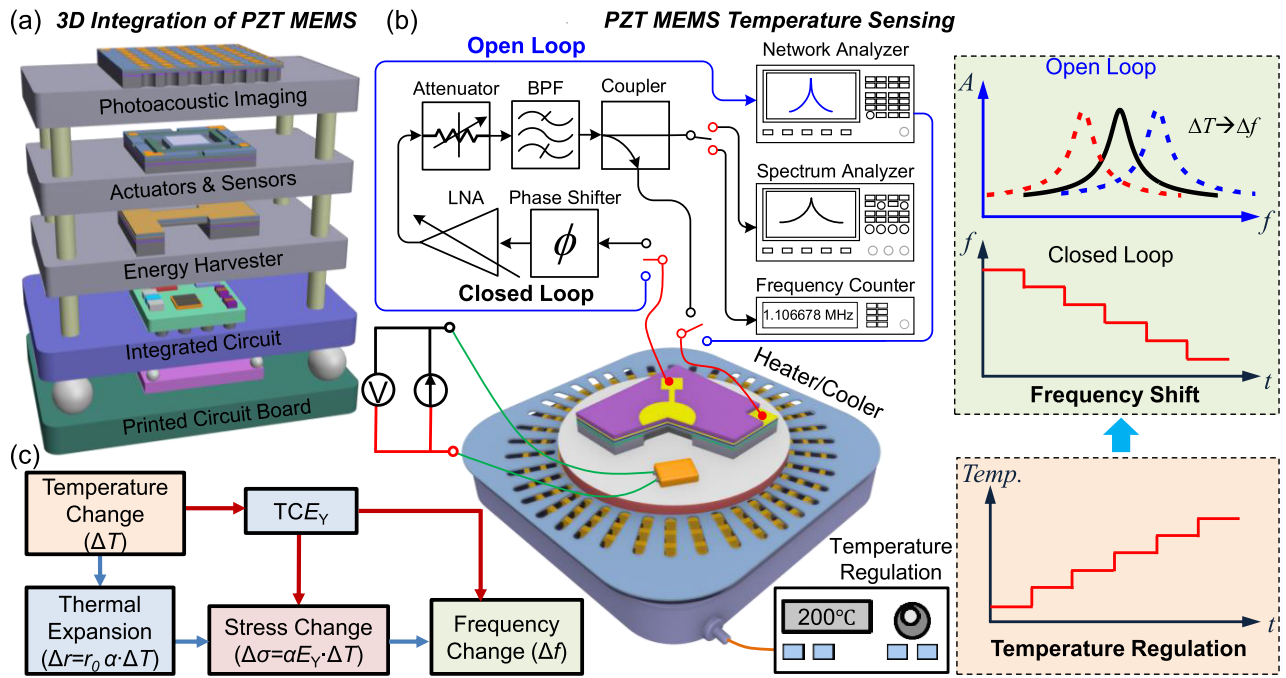


**Fig. 1.** Scientific background and experimental design. (a) Vision of future 3-D integration of PZT MEMS with ICs. (b) Device platform and measurement scheme for both open loop and closed loop, where BPF represents the bandpass filter, and LNA represents the low-noise amplifier. (c) Block diagram shows the effects of varying temperatures on the resonance frequency.  $TCE_Y$  represents the temperature coefficient of Young's modulus,  $\alpha$  is the thermal expansion coefficient, and  $r_0$  represents the initial radius.

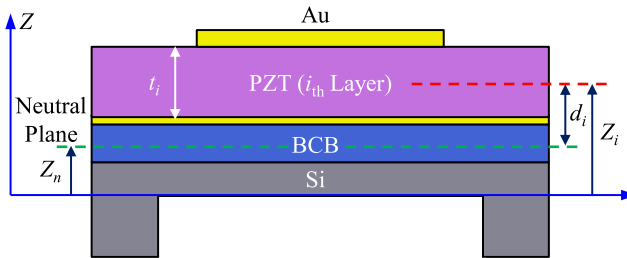


**Fig. 2.** Schematic of the cross-sectional view of the designed PZT MEMS.

**TABLE I**  
STRUCTURAL AND MATERIAL PROPERTIES

Structure	Material	Thickness [μm]	Young's Modulus [GPa]	Mass Density [kg/m³]	Poisson's Ratio
Supporting Layer	Si	3	170	2329	0.28
Bonding Layer	BCB	2	2.9	990	0.34
Bottom Electrode	Au	0.1	70	19300	0.44
Piezoelectric Layer	PZT	4	64	7870	0.31
Top Electrode	Au	0.35	70	19300	0.44

plane to the midplane of the  $i$ th layer. Table I summarizes the key properties of each structure layer. We first estimated the diameter of the device with (2) to obtain a device with a target frequency at 1.1 MHz. We then performed a finite-element method (FEM) simulation to guide the structural design. Starting from the calculated values, multiple iterations are performed in COMSOL Multiphysics to accurately find the corresponding device dimensions for the target frequencies. It has been found that the diaphragm with a diameter of 244  $\mu\text{m}$  yields the fundamental-mode resonant frequencies of 1.1 MHz.

The diameter of the top electrode is 172  $\mu\text{m}$ , which is designed with a 70% diameter coverage of the diaphragms for optimal transduction.

### B. Measurement Scheme

A customized heating and temperature sensing stage is utilized to precisely regulate the device's temperature, as shown in Fig. 1(b). We apply a resistive temperature sensor to the surface of either a metal ceramic heater element (25 °C to 211 °C) or a Peltier stage (0 °C to  $\sim$ 125 °C) utilizing nickel paste, to provide real-time monitoring of the heater's temperature. The MEMS die is then wired-bonded within a ceramic package, placed adjacent to the temperature sensor, and seated atop the heater. The highest temperature is well below the Curie temperature (242 °C) of PZT. Open-loop multimode resonances are measured by a network analyzer. Real-time tracking of the resonance frequency with temperature changing is achieved by either building a self-sustaining MEMS oscillator or a PLL. Fig. 1(c) shows the block diagram of temperature effects on the resonance frequency.

### III. FABRICATION OF PZT MEMS

The key fabrication processes of the PZT MEMS devices include temporary bonding of a ceramic PZT wafer to a Si wafer, CMP of ceramic PZT, and permanent bonding of a PZT thin film with an SOI wafer [38]. Fig. 3 shows the detailed fabrication process flow. First, the 500- $\mu\text{m}$ -thick ceramic PZT wafer was bonded with a Si wafer using BCB, and thinned down to 100  $\mu\text{m}$  with a smooth surface by CMP, followed by sputtering of 100-nm Au as the bottom electrode. After that, the PZT wafer was permanently bonded with an SOI wafer by BCB at 200 °C. Next, the PZT wafer was further thinned down to the designed thickness of 4  $\mu\text{m}$  by carefully removing the

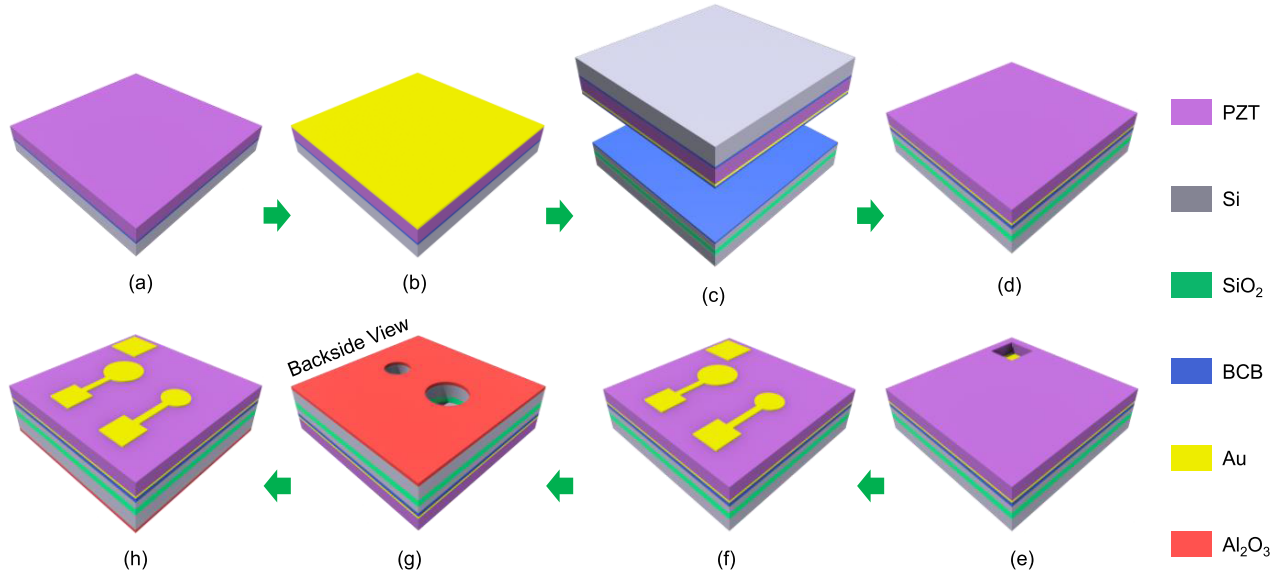


**Fig. 3.** Fabrication process flow of the PZT MEMS in this work. (a) Bond PZT wafer on a Si wafer and CMP. (b) Sputter Au. (c) Bond PZT wafer on an SOI wafer. (d) CMP PZT. (e) Wet etch PZT. (f) Define top Au electrode. (g) Backside etch Si and SiO<sub>2</sub>. (h) Final device on cavity.

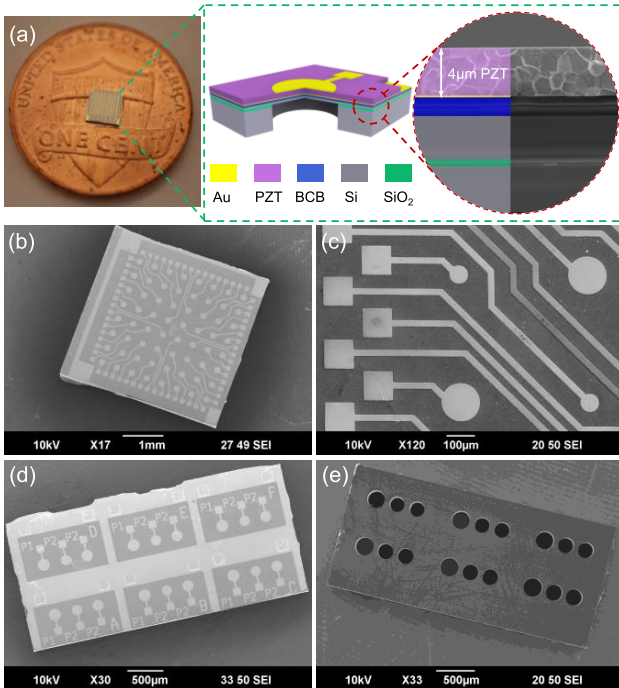


**Fig. 4.** (a) Optical image of the PZT MEMS chip and a cross-sectional view SEM of the multilayers. SEM images of (b) 8 × 8 PZT MEMS transducer array and (c) zoomed-in view of the top electrodes. SEM images of another chip with single elements in (d) front and (e) back side views, respectively.

Si, BCB, and PZT in sequence. The thin ceramic PZT was then patterned to expose the bottom electrode by wet etching with diluted fluoroboric acid ( $\text{HBF}_4$ ) [39]. Next, the top electrode pattern was defined by photolithography and formed by Au sputtering and liftoff process. Finally, the cavities were defined by a photolithography and a backside deep reactive-ion etching (DRIE) with an aluminum oxide ( $\text{Al}_2\text{O}_3$ ) layer as the hard mask. The  $\text{Al}_2\text{O}_3$  is patterned and wet etched by diluted hydrofluoric acid (HF).

Various devices with different chip sizes and a number of elements have been fabricated. Fig. 4(a) shows an optical image of a fabricated PZT MEMS chip with a size of  $3.5 \times 3.5$  mm. The inset shows the device structure and a cross-sectional view scanning electron microscopy (SEM) image, where the thickness of the ceramic PZT layer is measured to be around 4 μm. Fig. 4(b) shows an SEM image of a fabricated 8 × 8 PZT MEMS transducer array, whose top electrodes are shown in a zoomed-in view of SEM image in Fig. 4(c). Fig. 4(d) and (e) shows the SEM images of another fabricated chip with single elements in the front and back side views, respectively.

## IV. RESULTS AND DISCUSSION

### A. Temperature-Dependent Multimode Resonances

We first characterize the multimode resonances of circular diaphragm PZT MEMS resonators with a diameter of 244 μm, at 25 °C, by using a network analyzer [Fig. 5(a)]. Three resonance modes are observed in the range of 1 to 8 MHz,  $f_1 = 1.107$  MHz,  $f_2 = 3.620$  MHz, and  $f_3 = 6.778$  MHz. For fundamental mode, the device has a  $Q$  factor of 50 both in air and in vacuum with a pressure of 50 mTorr. The FEM simulated resonance frequencies match the measurement well, with  $f_{S1} = 1.109$  MHz,  $f_{S2} = 3.698$  MHz, and  $f_{S3} = 6.794$  MHz, and the corresponding mode shapes are shown in Fig. 5(b).

To determine the temperature coefficient of resonance frequency, we measure these modes in the temperature range of 25 °C to 211 °C. The MEMS device chip is mounted in a ceramic package and faced the heater. The resonance frequencies of the three modes are recorded. Fig. 5(c) shows the resonance spectrum of the PZT MEMS at 25 °C and 211 °C, respectively. TC $f$  values are evaluated by using

$$\text{TC}f = \frac{1}{f} \frac{\Delta f}{\Delta T} \quad (6)$$

where  $T$  is the temperature. We find that the resonance frequencies decrease monotonically with increasing temperature (Fig. 6). We plot the frequency shift at different temperatures

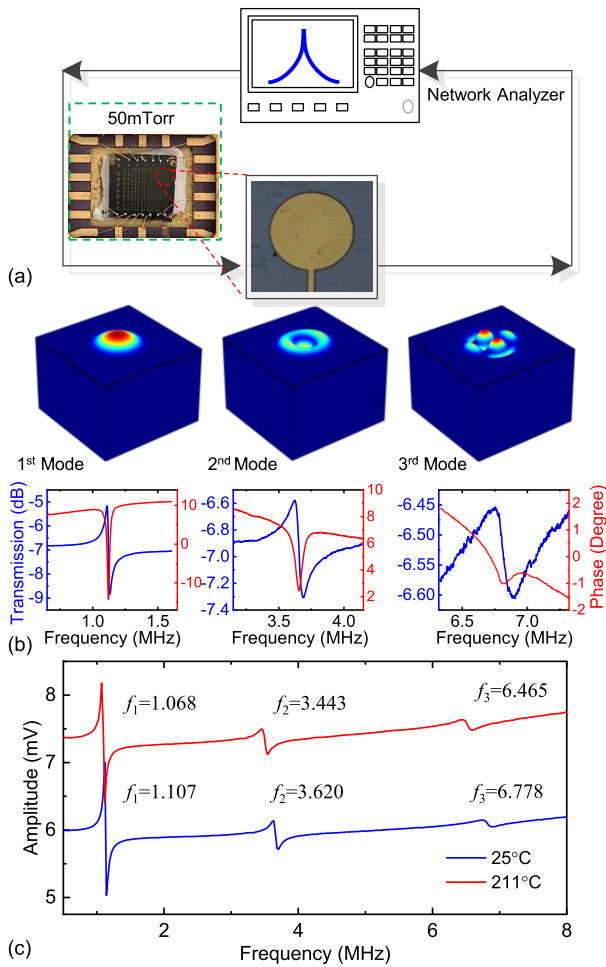


**Fig. 5.** (a) Schematic of open-loop measurement, with a photograph of PZT MEMS dies wire bonded in a ceramic package and a zoomed-in view of a single device with a diameter of 244  $\mu\text{m}$ . (b) Multimode resonance was measured at room temperature (25  $^{\circ}\text{C}$ ) and the corresponding mode shapes were simulated in COMSOL. (c) Resonance spectra measured in the range from 0.5 to 8 MHz at 25  $^{\circ}\text{C}$  and 211  $^{\circ}\text{C}$ , respectively.

with respect to its resonance frequency at 25  $^{\circ}\text{C}$  for each of the three modes, in which a linear relation between  $\Delta f/f$  and  $T$  is observed from each mode. We then extract an average  $\text{TC}f_1 = -193 \text{ ppm}/^{\circ}\text{C}$  for the first mode,  $\text{TC}f_2 = -268 \text{ ppm}/^{\circ}\text{C}$  for the second mode, and  $\text{TC}f_3 = -255 \text{ ppm}/^{\circ}\text{C}$  for the third mode. The linear temperature dependence and  $\text{TC}f$  values of the PZT MEMS resonator can be directly exploited for on-chip temperature sensing.

Starting from (2),  $\text{TC}f$  of a circular diaphragm operating in the plate regimes can be approximately expressed as follows:

$$\text{TC}f \approx \frac{3}{2}\alpha + \frac{\text{TCE}_Y}{2} \quad (7)$$

where  $\alpha$  is the thermal expansion coefficient, and  $\text{TCE}_Y$  is the temperature coefficient of Young's modulus. Thus, the monotonic decrease of resonance frequencies is determined by the synergistic effects of thermal expansion and temperature-dependent Young's modulus. In our case, we should consider the effective thermal expansion coefficient ( $\alpha_{\text{eff}}$ ) and effective  $\text{TCE}_Y$  of the multilayer structure, which makes it more complicated. As reported, the thermal expansion coefficient of Si and Au changes only slightly over a wide temperature

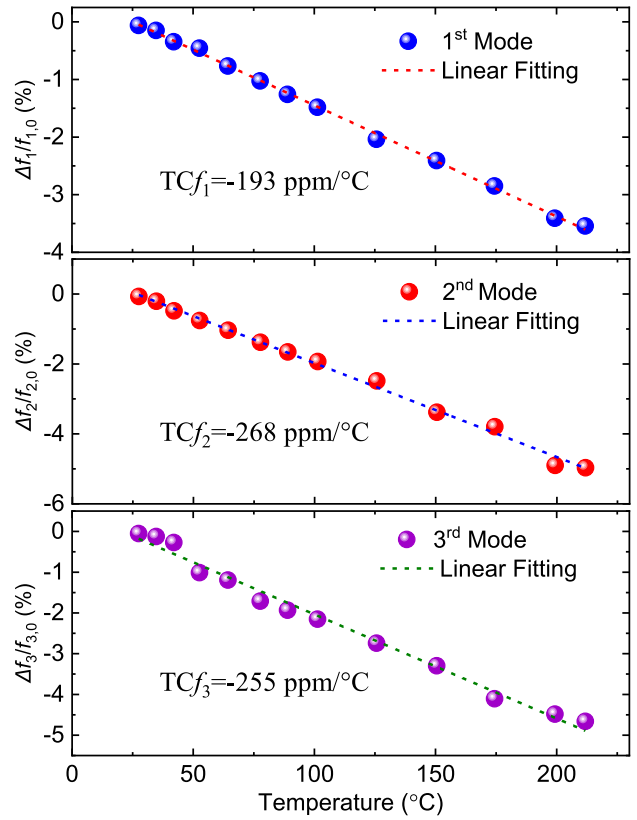


**Fig. 6.** Fractional frequency shift measured from the three modes versus varying temperature from 25  $^{\circ}\text{C}$  to 211  $^{\circ}\text{C}$ , with  $\text{TC}f$  extraction.

range [40], [41], indicating that they do not play a major role in determining the  $\text{TC}f$ . On the other hand, Young's modulus of these materials decreases more noticeably with increasing temperature [42], [43]. It is, therefore, reasonable to suggest that the monotonic decrease of resonance frequencies is dominated by the effective  $\text{TCE}_Y$  of the heterostructure stack.

### B. Self-Sustaining MEMS Oscillator

To enable real-time tracking of the resonance frequency, we need to build a self-sustaining oscillator and do closed-loop measurements. However, the large electrical background arising from parasitic effects and impedance mismatch makes it difficult to satisfy the Barkhausen criteria at the resonance frequency [44], particularly when the frequency strongly shifts with temperature. Fig. 7 shows the equivalent circuit model of the PZT MEMS, and the simulated resonance in Cadence. A large feedthrough capacitance ( $C_f$ ) of 141 pF is extracted, which may originate from the global bottom electrode for all the devices on the chip. To nullify the electrical background and enable higher signal-to-background ratios, we build a balanced bridge circuit with two devices operating at different frequencies but with similar electrical backgrounds on the same chip. Fig. 8(a) shows the bridge circuit, which primarily consists of a 180  $^{\circ}$  phase shifter and an attenuator. By carefully adjusting the attenuator, the electrical background can be effectively minimized [Fig. 8(b)].

We then build a self-sustaining MEMS oscillator using the PZT MEMS resonator with the diagram shown in Fig. 1(b). We first perform an open-loop measurement to calibrate

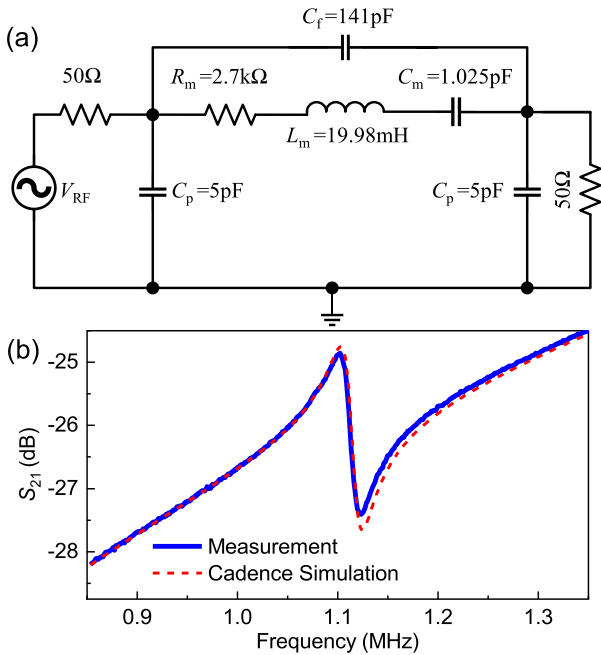


**Fig. 7.** (a) Equivalent circuit model of the PZT MEMS and (b) simulated resonance response, which matches the measurement well.

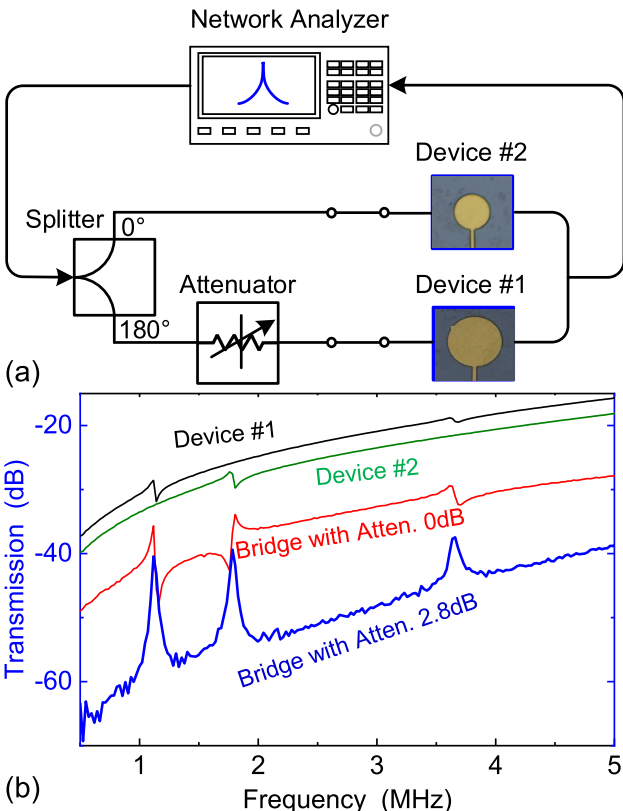


**Fig. 8.** (a) Balanced bridge circuit scheme. (b) Measured resonance spectra for Devices 1 and 2, and the balanced bridge with the attenuator set at 0 and 2.8 dB, respectively.

on meeting the Barkhausen criteria [44], with the overall open-loop gain slightly greater than 0 dB near the resonance frequency, and the overall phase shift to be  $2n\pi$ , where  $n$  is an integer. After satisfying the Barkhausen criteria, we close

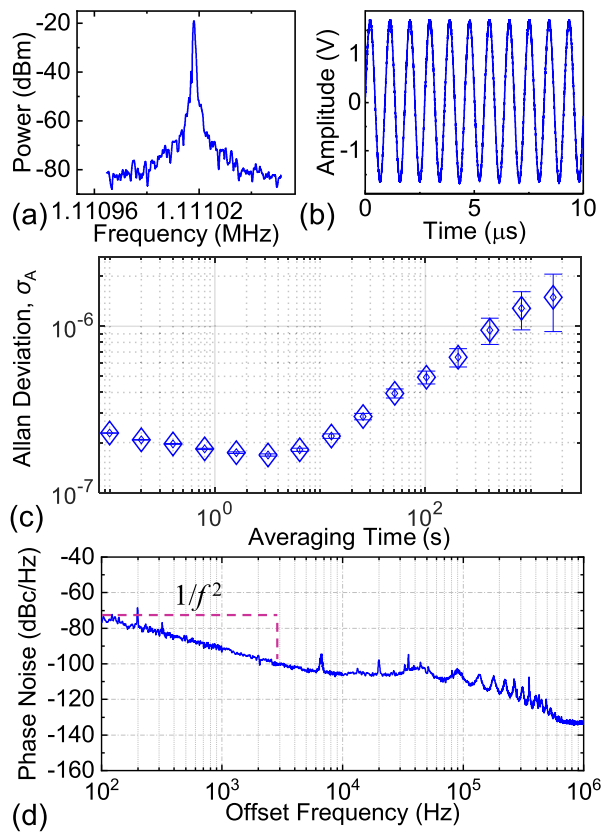


**Fig. 9.** Self-sustaining PZT MEMS oscillator characteristics from measurements. (a) Oscillator output spectrum. (b) Time-domain waveform. (c) Phase noise. (d) Allan deviation.

the loop and measure the stable self-oscillation both in the frequency domain and time domain [Fig. 9(a) and (b)]. We characterize the oscillator's performance by measuring its frequency stability. From the time-domain tracked frequency data trace, we calculate the Allan deviation [45] [Fig. 9(c)] from

$$\sigma_A(\tau_A) = \left[ \frac{1}{2(N-1)} \sum_{i=1}^{N-1} \left( \frac{\bar{f}_{i+1} - \bar{f}_i}{f_0} \right)^2 \right]^{1/2} \quad (8)$$

where  $\bar{f}_i$  is the measured average frequency in the  $i$ th discrete time interval of  $\tau_A$ . The Allan deviation data gives us the short-term frequency stability  $\sigma_A \approx 2 \times 10^{-7}$  at averaging time  $\tau_A < 5$  s, and long-term frequency stability  $\sigma_A \approx 1 \times 10^{-6}$  at  $\tau_A = 1000$  s [Fig. 9(c)]. We then examine the phase noise behavior using the phase noise module in a spectrum analyzer. In the phase noise plot, we see two main regions. Phase noise first decreases in the 100 Hz to 8 kHz range, largely following a  $1/f^2$  power law, suggesting it is dominated by thermal noise. Phase noise flattens out beyond 10-kHz offset frequency and then decreases again [Fig. 9(d)].

### C. Closed-Loop $TC_f$

To further explore the temperature-dependent resonance of the PZT MEMS, we have done closed-loop  $TC_f$  measurement on the self-sustaining oscillator. We gradually increase the voltage applied to the ceramic heater from 0 to 9 V [Fig. 10(a)]. The resistance of the commercial resistive temperature sensor increases from 109 to 150 Ω, corresponding

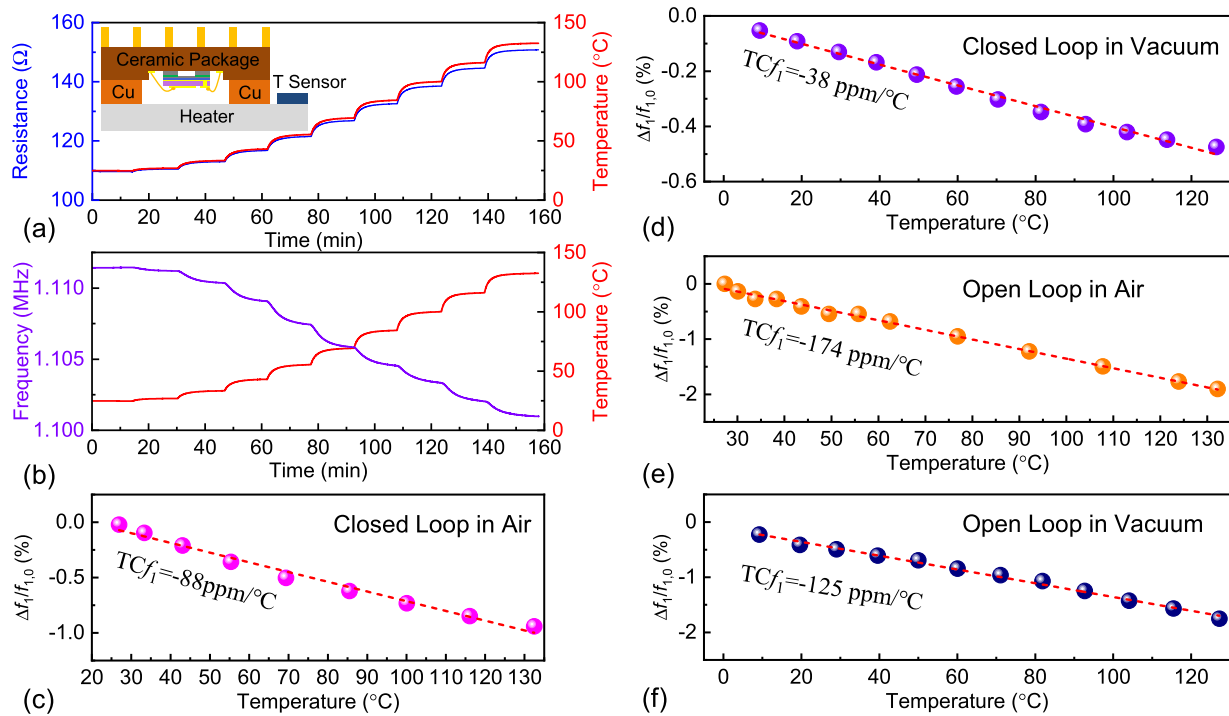


**Fig. 10.** TCf measured in different scenarios. (a) Resistance and temperature are read from a resistive temperature sensor. Inset: Diagram illustrating the arrangement of the heater, temperature sensor, MEMS, and Cu cushion. (b) Real-time tracking of the frequency of the self-sustaining oscillator. (c) Fractional frequency shift ( $\Delta f_1/f_{1,0}$ ) with varying temperature extracted from closed-loop measurement in air, where reference frequency  $f_{1,0}$  is the frequency measured at room temperature. The averaged TCf is obtained by linear fitting of the  $\Delta f_1/f_{1,0}$  versus temperature plot. (d) Closed-loop TCf in 50-mTorr vacuum. (e) Open-loop TCf in air. (f) Open-loop TCf in 50-mTorr vacuum.

to a change of temperature from 25 °C to 132 °C. Fig. 10(b) shows the frequency variation versus time. The PZT MEMS devices respond rapidly to the changes in temperature. However, it takes  $\sim 15$  min for the frequency to be stabilized. This could be attributed to at least two factors. One effect may be caused by the slow heating process of the ceramic heater. Another may result from the slow heat transfer from the heater to the MEMS devices.

To better understand the temperature-dependent resonance of the PZT device, we conduct and compare the TCf measured in different scenarios, i.e., different mounting schemes, in air or vacuum, and closed loop or open loop. To improve thermal conduction and safeguard the wires, we add a slim Cu cushion between the heater and the ceramic package. Then, raising the temperature of the heater results in a prompt response from the temperature sensor and a corresponding rapid response from the MEMS device frequency in all scenarios. This simultaneous quick response from both resistance and frequency is indicative of swift heat transfer. To extract TCf, we take the temperature and frequency values after both are stabilized. The fractional downshift of the resonance frequency for the first mode ( $\Delta f_1/f_{1,0}$ ) measured in different scenarios are shown in Fig. 10(c) and (e) and the extracted TCf<sub>1</sub> values are summarized in Table II.

The absolute open-loop TCf<sub>1</sub> decreases from 193 to 174 ppm/°C when the gap increases by 1 mm by adding the Cu cushion, as shown in the inset of Fig. 10(a), which may result from the lower heating efficiency. The absolute TCf<sub>1</sub> measured in air is  $\sim 50$  ppm/°C larger than that measured in vacuum in both open-loop and closed-loop configurations. This indicates

**TABLE II**  
TCf MEASURED FROM PZT MEMS DEVICES

Modality	Heater	Cushion	Pressure	Temperature [°C]	TCf <sub>1</sub> [ppm/°C]
Resonator	Ceramic	No	Air	25 to 211	-193
Resonator	Ceramic	Yes	Air	25 to 132	-174
Resonator	Peltier	Yes	50mTorr	0 to 125	-125
Oscillator	Ceramic	Yes	Air	25 to 132	-88
Oscillator	Peltier	Yes	50mTorr	0 to 125	-38

that the heat convection has been suppressed by removing air molecules. By means of the processes of heat convection and conduction, the heater will transfer heat to the MEMS chip through the air trapped in the narrow space (totally  $\sim 2$ -mm gap) between the heater and the chip. In a vacuum of 50 mTorr, however, heat convection has been suppressed, which further lowers the actual temperature of the MEMS chip than that read from the commercial temperature sensor attached directly on top of the heater [ $T_{\text{MEMS in Air}} < T_{\text{Sensor}}$  and  $T_{\text{MEMS in Vacuum}} < T_{\text{MEMS in Air}} < T_{\text{Sensor}}$ , where  $T_{\text{Sensor}}$  is the temperature read from the commercial temperature sensor, see inset of Fig. 10(a)]. This further leads to a smaller change in the resonance frequency ( $\Delta f_{\text{Vacuum}} < \Delta f_{\text{Air}}$ ) and smaller measured TCf<sub>1</sub> in the case of vacuum.

Note that the absolute TCf<sub>1</sub> values extracted from the closed loop are lower than that obtained from the open loop. Such difference in TCf<sub>1</sub> measured from open-loop and closed-loop configurations has also been reported in the AlN solid-mounted resonator [46], which can be attributed to

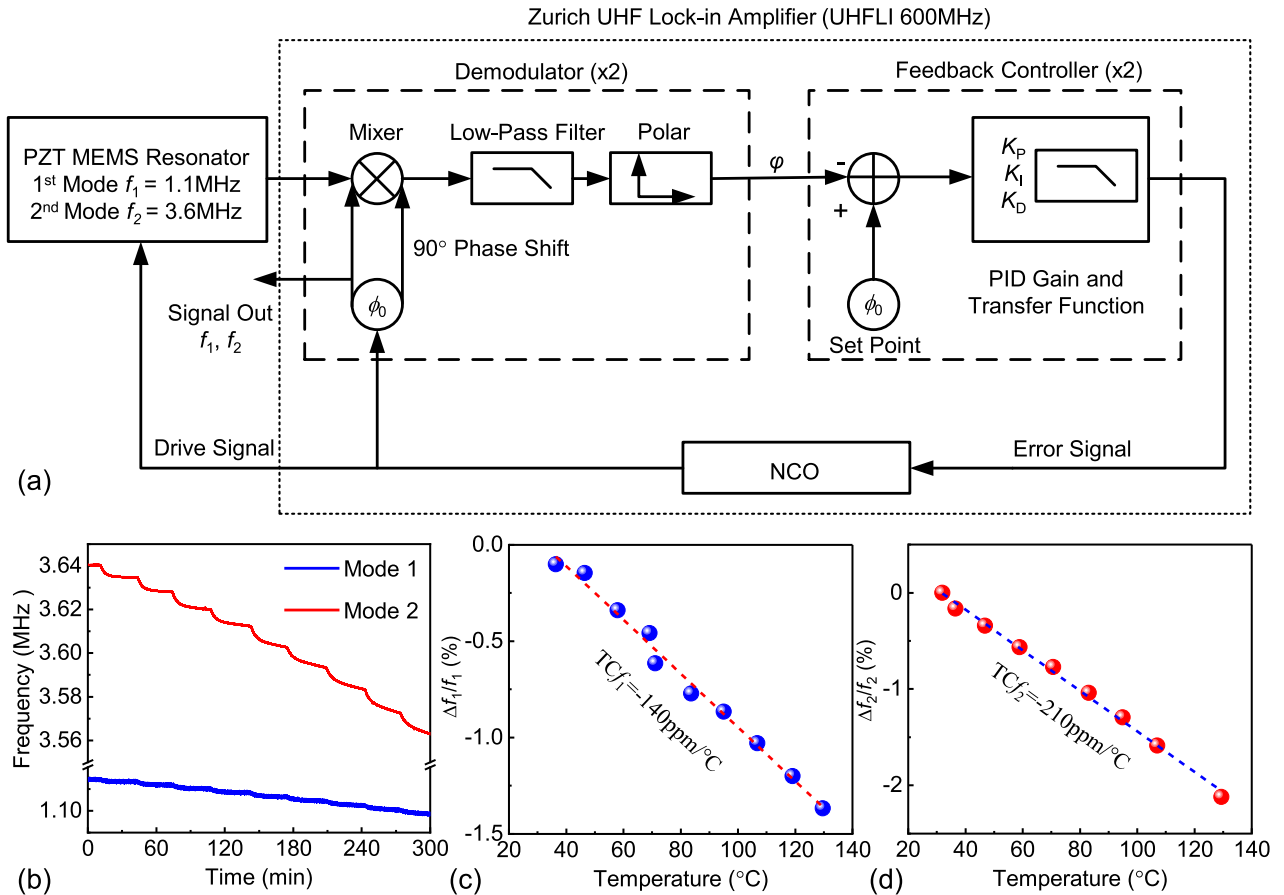


**Fig. 11.** Dual-mode frequency tracking by PLL. (a) PLL circuit diagram. (b) Real-time tracking of the dual-mode resonance frequency using Zurich UHFLI 600-MHz lock-in amplifier. (c) Fractional frequency shift ( $\Delta f_1/f_{1,0}$ ) with varying temperature, where  $f_{1,0}$  is the fundamental-mode resonance frequency measured at room temperature. The averaged  $TCf_1$  is obtained by linear fitting of  $\Delta f_1/f_{1,0}$  versus temperature plot. (d) Fractional frequency shift ( $\Delta f_2/f_{2,0}$ ) with varying temperature, where  $f_{2,0}$  is the second mode resonance frequency measured at room temperature. The averaged  $TCf_2$  is obtained by linear fitting of  $\Delta f_2/f_{2,0}$  versus temperature plot.

the temperature instability of the electronics composing the oscillator. However, in our work, only the MEMS resonator is heated within the loop. The detailed mechanisms causing the difference between open-loop  $TCf$  and closed-loop  $TCf$  necessitates further investigation.

#### D. Dual-Mode Frequency Tracking by PLL

Multimode resonances have been exploited to resolve the position and mass of nanoparticles with high throughput and high resolution [47], [48]. The dual-mode oscillation scheme has been demonstrated as an effective method for achieving precise temperature sensing across a wide temperature range. In a particular device with the first and second modes simultaneously excited, the resulting beat frequency (i.e., the difference between the two frequencies) can provide an accurate measure of the resonator's response to temperature changes. Because both modes are produced by the same resonator, any relative changes in their  $TCfs$  are inherently linked. As a result, any higher order variations in one mode will be mirrored in the other, creating a near-linear function of temperature with respect to the beat frequency. For example, it is worth noting that mass loading resulting from random particle deposition on the device can cause a nonlinear decrease in the frequencies of the two modes as temperature increases.

However, by relying on the beat frequency of these two modes, it is possible to effectively decouple the effects of mass loading from the resonator's temperature response.

PZT MEMS resonator demonstrated in this work exhibits large absolute  $TCf$  values exceeding 200 ppm/ $^\circ\text{C}$  for the first three modes, showcasing its strong potential for on-chip temperature sensing with high resolution. To validate its feasibility, we further demonstrate the dual-mode frequency tracking by PLL in real time. In a PLL, the output of a low-noise oscillator [numerically controlled oscillator (NCO)] which generates the reference signal in Fig. 11(a)] is locked in phase and frequency with the input signal [output from PZT MEMS in Fig. 11(a)] through a feedback control mechanism. It compares the phase of the input signal with that of the reference signal and then shifts the phase of the output signal [error signal in Fig. 11(a)] to match the input signal. PLLs are commonly used in radio frequency and microwave applications to lock local oscillators to signals from remote transmitters, and in other applications, such as clock synchronization, frequency synthesis, and signal modulation. For sensing applications, PLL is used to stabilize and follow the input signal's resonance frequency. It is extensively used for tracking micro/nanomechanical vibrations [48], [49], [50], [51], [52] and atomic force microscopy [53]. Here, we employ PLL to track frequency shifts for performing the frequency

stability measurements as well as for tracking real-time multimode frequency shifts caused by temperature change.

**Fig. 11(a)** demonstrates the PLL circuit diagram, which originally takes advantage of the built-in functionality of the Zurich Instruments UHFLI 600MHz lock-in amplifier. A dual-phase demodulator, proportional–integral–derivative (PID) controller and an NCO are the basic building blocks of a PLL inside the UHFLI 600MHz lock-in amplifier. These form a negative feedback loop, and the mixer (phase detector) detects the phase difference between the signal from the MEMS device and the reference oscillator. The PZT MEMS under test in the Zurich instrument serves as the frequency-determining element of the circuit, with the PID feedback controller regulating the frequency of the NCO. The transfer function for the error signal is determined by the PID gains, which are in turn controlled by the feedback controller and the PID parameters. The transfer function begins to filter out fluctuations with a time scale that is less than the corner frequency. Based on mechanical  $Q$ , center frequency, required PLL bandwidth, locking range, and phase setpoint, the lock-in “advisor” program automatically calculates the PID settings. The “advisor” uses a first-order transfer function simulation to compute a set of feedback gain parameters that it predicts to best match the specified bandwidth. This is accomplished by employing a numerically optimized technique for loop dynamics.

We employ two demodulators and two PID controllers to perform dual-mode PLL measurement with the device in 50-mTorr vacuum. The dual mode (first mode and second mode) frequency shifts of the PZT device are measured simultaneously by increasing the temperature from 25 to 132 °C [**Fig. 11(b)**]. The fractional frequency shifts of the two modes with varying temperatures are shown in **Fig. 11(c)** and **(d)**. We find that the second mode’s frequency shift is higher than the first mode with the same temperature change which signifies that the second mode has a higher TC $f$  compared to the first mode. This is also consistent with the open-loop TC $f$  measurement shown in **Fig. 6**. The average TC $f$ s of the two modes are obtained by linear fitting of the fractional frequency shifts with temperature change which yields TC $f_1 = -140$  ppm/°C and TC $f_2 = -210$  ppm/°C. Interestingly, the absolute TC $f$ s of the two modes measured from PLL in 50 mTorr vacuum are ~50 ppm/°C lower than that obtained from open-loop measurements in the air (with TC $f_1 = -193$  ppm/°C and TC $f_2 = -268$  ppm/°C). As discussed before, this may be related to the suppressed heat transfer by removing air molecules trapped in the small gap between the heater and MEMS chip [see **Fig. 10(a)** inset].

## V. CONCLUSION

In conclusion, we have experimentally demonstrated an integrated multimode resonant MEMS temperature sensor by exploiting a thin film ceramic PZT piezoelectric micromachined transducers in the megahertz range. We have designed and fabricated the PZT MEMS transducers operating in flexural mode by using wafer bonding and CMP techniques. All three resonance modes exhibit excellent linearity and high responsivity to temperature variations from 25 °C to 211 °C, with TC $f \sim -200$  ppm/°C to -270 ppm/°C for open-loop measurement. A balanced bridge circuit with two devices on the same chip is built to nullify the electrical background and enable higher signal-to-background ratios. We have demonstrated temperature sensing with real-time

tracking of the resonance frequency using a PLL. We have built a self-sustaining PZT MEMS oscillator and measured the closed-loop TC $f$  in different scenarios. The absolute TC $f$  measured in air is ~50 ppm/°C larger than that measured in vacuum in both open-loop and closed-loop configurations, which indicates that heat convection and conduction have been suppressed by removing air molecules.

## REFERENCES

- [1] S. Fan, R. Wei, L. Zhao, X. Yang, L. Geng, and P. X.-L. Feng, “An ultralow quiescent current power management system with maximum power point tracking (MPPT) for batteryless wireless sensor applications,” *IEEE Trans. Power Electron.*, vol. 33, no. 9, pp. 7326–7337, Sep. 2018.
- [2] S. Fan et al., “mm-scale and MEMS piezoelectric energy harvesters powering on-chip CMOS temperature sensing for IoT applications,” in *Proc. 19th Int. Conf. Solid-State Sensors, Actuat. Microsyst.*, Jun. 2017, pp. 1848–1850.
- [3] R. Wei, A. Boggis, S. Maley, and P. X.-L. Feng, “Self-powering wireless sensors for temperature sensing and monitoring in power generation applications,” *Proc. SPIE*, vol. 10970, Mar. 2019, Art. no. 109700V.
- [4] H.-C. Lee and K.-H. Ke, “Monitoring of large-area IoT sensors using a LoRa wireless mesh network system: Design and evaluation,” *IEEE Trans. Instrum. Meas.*, vol. 67, no. 9, pp. 2177–2187, Sep. 2018.
- [5] A. I. Sunny, A. Zhao, L. Li, and S. K. Kanthek Sakiliba, “Low-cost IoT-based sensor system: A case study on harsh environmental monitoring,” *Sensors*, vol. 21, no. 1, p. 214, Dec. 2020.
- [6] W. Sui et al., “Effects of ion-induced displacement damage on GaN/AlN MEMS resonators,” *IEEE Trans. Nucl. Sci.*, vol. 69, no. 3, pp. 216–224, Mar. 2022.
- [7] J. Yang, “A harsh environment wireless pressure sensing solution utilizing high temperature electronics,” *Sensors*, vol. 13, no. 3, pp. 2719–2734, Feb. 2013.
- [8] A. Ghosh, C. Zhang, S. Q. Shi, and H. Zhang, “High-Temperature gas sensors for harsh environment applications: A review,” *CLEAN-Soil, Air, Water*, vol. 47, no. 8, Aug. 2019, Art. no. 1800491.
- [9] X. Q. Bao, W. Burkhard, V. V. Varadan, and V. K. Varadan, “SAW temperature sensor and remote reading system,” in *Proc. IEEE Ultrason. Symp.*, Denver, CO, USA, Mar. 1987, pp. 583–586.
- [10] S. Ren, W. Yuan, D. Qiao, J. Deng, and X. Sun, “A micromachined pressure sensor with integrated resonator operating at atmospheric pressure,” *Sensors*, vol. 13, no. 12, pp. 17006–17024, Dec. 2013.
- [11] T. Ueda, F. Kohsaka, T. Iino, and D. Yamazaki, “Temperature sensor using quartz tuning fork resonator,” in *Proc. 40th Annu. Symp. Freq. Control*, Philadelphia, PA, USA, 1986, pp. 224–229.
- [12] H. Fatemi, M. J. Modarres-Zadeh, and R. Abdolvand, “Passive wireless temperature sensing with piezoelectric MEMS resonators,” in *Proc. 28th IEEE Int. Conf. Micro Electro Mech. Syst. (MEMS)*, Jan. 2015, pp. 909–912.
- [13] P. Song et al., “Recent progress of miniature MEMS pressure sensors,” *Micromachines*, vol. 11, no. 1, p. 56, Jan. 2020.
- [14] K. Park, N. Kim, D. T. Morissette, N. R. Aluru, and R. Bashir, “Resonant MEMS mass sensors for measurement of microdroplet evaporation,” *J. Microelectromech. Syst.*, vol. 21, no. 3, pp. 702–711, Jun. 2012.
- [15] J. Xu, M. Bertke, H. S. Wasisto, and E. Peiner, “Piezoresistive microcantilevers for humidity sensing,” *J. Micromech. Microeng.*, vol. 29, no. 5, Apr. 2019, Art. no. 053003.
- [16] W. Sui, H. Wang, J. Lee, A. Qamar, M. Rais-Zadeh, and P. X. Feng, “AlScN-on-SiC thin film micromachined resonant transducers operating in high-temperature environment up to 600 °C,” *Adv. Funct. Mater.*, vol. 32, no. 34, Aug. 2022, Art. no. 2202204.
- [17] A. Qamar, S. R. Eisner, D. G. Senesky, and M. Rais-Zadeh, “Ultra-high-Q gallium nitride SAW resonators for applications with extreme temperature swings,” *J. Microelectromech. Syst.*, vol. 29, no. 5, pp. 900–905, Oct. 2020.
- [18] W. Sui, X.-Q. Zheng, J.-T. Lin, B. W. Alphenaar, and P. X.-L. Feng, “Thermal response and TC  $f$  of GaN/AlN heterostructure multimode micro string resonators from -10 °C up to 325 °C,” *J. Microelectromech. Syst.*, vol. 30, no. 4, pp. 521–529, Aug. 2021.
- [19] J. Strelc et al., “Design and characterization of high-Q SAW resonators based on the AlN/sapphire structure intended for high-temperature wireless sensor applications,” *IEEE Sensors J.*, vol. 20, no. 13, pp. 6985–6991, Jul. 2020.

- [20] J. Yang, B. Hamelin, and F. Ayazi, "Investigating elastic anisotropy of 4H-SiC using ultra-high  $q$  bulk acoustic wave resonators," *J. Microelectromech. Syst.*, vol. 29, no. 6, pp. 1473–1482, Dec. 2020.
- [21] Q. Xie et al., "Effectiveness of oxide trench array as a passive temperature compensation structure in AlN-on-silicon micromechanical resonators," *Appl. Phys. Lett.*, vol. 110, no. 8, Feb. 2017.
- [22] M. Reusch, K. Holc, V. Lebedev, N. Kurz, A. Žukauskaite, and O. Ambacher, "Temperature cross-sensitivity of AlN-based flexural plate wave sensors," *IEEE Sensors J.*, vol. 18, no. 19, pp. 7810–7818, Oct. 2018.
- [23] S. Fei and H. Ren, "Temperature characteristics of a contour mode MEMS AlN piezoelectric ring resonator on SOI substrate," *Micromachines*, vol. 12, no. 2, p. 143, Jan. 2021.
- [24] A. K. Samara and F. Ayazi, "Temperature compensation of silicon micromechanical resonators via degenerate doping," in *IEDM Tech. Dig.*, Baltimore, MD, USA, Dec. 2009, pp. 1–4.
- [25] A. Hajjam, A. Logan, and S. Pourkamali, "Doping-induced temperature compensation of thermally actuated high-frequency silicon micromechanical resonators," *J. Microelectromech. Syst.*, vol. 21, no. 3, pp. 681–687, Jun. 2012.
- [26] M. Moosavifar, A. Ansari, and M. Rais-Zadeh, "An AlN-on-Si resonant IR sensor array with a large temperature coefficient of frequency," in *Proc. IEEE Sensors*, Orlando, FL, USA, Jul. 2016, pp. 1–3.
- [27] W. Sui, X.-Q. Zheng, J.-T. Lin, B. W. Alphenaar, and P. X.-L. Feng, "Temperature dependence of multimode gallium nitride/aluminum nitride (GaN/AlN) heterostructure string resonator," in *Proc. IEEE 34th Int. Conf. Micro Electro Mech. Syst. (MEMS)*, Gainesville, FL, USA, Jan. 2021, pp. 478–481.
- [28] A. C. Fischer et al., "Integrating MEMS and ICs," *Microsyst. Nanoeng.*, vol. 1, no. 1, pp. 1–16, May 2015.
- [29] C. G. Hindrichsen, R. Lou-Møller, K. Hansen, and E. V. Thomsen, "Advantages of PZT thick film for MEMS sensors," *Sens. Actuators A, Phys.*, vol. 163, no. 1, pp. 9–14, Sep. 2010.
- [30] G. L. Smith et al., "PZT-based piezoelectric MEMS technology," *J. Amer. Ceram. Soc.*, vol. 95, no. 6, pp. 1777–1792, Jun. 2012.
- [31] M. D. Nguyen, H. N. Vu, D. H. Blank, and G. Rijnders, "Epitaxial Pb(Zr,Ti)O<sub>3</sub> thin films for a MEMS application," *Adv. Nat. Sci.*, vol. 2, no. 1, Mar. 2011, Art. no. 015005.
- [32] H. Wang, P. X.-L. Feng, and H. Xie, "A high-density and dual-frequency PMUT array based on thin ceramic PZT for endoscopic photoacoustic imaging," in *Proc. IEEE 34th Int. Conf. Micro Electro Mech. Syst. (MEMS)*, Gainesville, FL, USA, Jan. 2021, pp. 891–894.
- [33] H. Wang, H. Yang, H. Jiang, Z. Chen, P. X.-L. Feng, and H. Xie, "A multi-frequency pMUT array based on ceramic PZT for endoscopic photoacoustic imaging," in *Proc. 21st Int. Conf. Solid-State Sensors, Actuat. Microsyst.*, Jun. 2021, pp. 30–33.
- [34] A. Dangi et al., "Evaluation of high frequency piezoelectric micromachined ultrasound transducers for photoacoustic imaging," in *Proc. IEEE Sensors*, New Delhi, India, Oct. 2018, pp. 1–4.
- [35] H. Ahn, M. Sung, K. Been, and W. Moon, "Piezoelectric micromachined ultrasound array transducer with 31 channels for photoacoustic imaging," in *Proc. IEEE Int. Ultrason. Symp.*, Barcelona, Spain, Sep. 2014, pp. 1831–1834.
- [36] E. E. Aktakka, R. L. Peterson, and K. Najafi, "Wafer-level integration of high-quality bulk piezoelectric ceramics on silicon," *IEEE Trans. Electron Devices*, vol. 60, no. 6, pp. 2022–2030, Jun. 2013.
- [37] H. Suzuki, N. Yamaguchi, and H. Izumi, "Theoretical and experimental studies on the resonance frequencies of a stretched circular plate: Application to Japanese drum diaphragms," *Acoust. Sci. Technol.*, vol. 30, no. 5, pp. 348–354, 2009.
- [38] W. Sui et al., "Thin film PZT multimode resonant MEMS temperature sensor," in *Proc. IEEE Sensors*, Dallas, TX, USA, Oct. 2022, pp. 1–4.
- [39] H. Wang, M. Godara, Z. Chen, and H. Xie, "A one-step residue-free wet etching process of ceramic PZT for piezoelectric transducers," *Sens. Actuators A, Phys.*, vol. 290, pp. 130–136, May 2019.
- [40] U. Köbler, "The importance of the Debye bosons (sound waves) for the lattice dynamics of solids," *Int. J. Thermodyn.*, vol. 23, no. 2, pp. 59–79, May 2020.
- [41] H. Watanabe, N. Yamada, and M. Okaji, "Linear thermal expansion coefficient of silicon from 293 to 1000 K," *Int. J. Thermophys.*, vol. 25, no. 1, pp. 221–236, Jan. 2004.
- [42] C. Birleanu et al., "Temperature effect on the mechanical properties of gold nano films with different thickness," *IOP Conf. Ser. Mater. Sci. Eng.*, vol. 147, no. 1, Aug. 2016, Art. no. 012021.
- [43] J. Vanhellemont, A. K. Swarnakar, and O. Van der Biest, "Temperature dependent Young's modulus of Si and Ge," *ECS Trans.*, vol. 64, no. 11, pp. 283–292, Aug. 2014.
- [44] X. L. Feng, C. J. White, A. Hajimiri, and M. L. Roukes, "A self-sustaining ultrahigh-frequency nanoelectromechanical oscillator," *Nature Nanotechnol.*, vol. 3, no. 6, pp. 342–346, May 2008.
- [45] D. W. Allan, "Time and frequency (time-domain) characterization, estimation, and prediction of precision clocks and oscillators," *IEEE Trans. Ultrason., Ferroelectr., Freq. Control*, vol. UFFC-34, no. 6, pp. 647–654, Nov. 1987.
- [46] M. Rinaldi, A. Tazzoli, J. Segovia-Fernandez, V. Felmetser, and G. Piazza, "High power and low temperature coefficient of frequency oscillator based on a fully anchored and oxide compensated ALN contour-mode MEMS resonator," in *Proc. IEEE 25th Int. Conf. Micro Electro Mech. Syst. (MEMS)*, Jan. 2012, pp. 696–699.
- [47] M. S. Hanay, S. I. Kelber, C. D. O'Connell, P. Mulvaney, J. E. Sader, and M. L. Roukes, "Inertial imaging with nanomechanical systems," *Nature Nanotechnol.*, vol. 10, no. 4, pp. 339–344, Apr. 2015.
- [48] S. Olcum, N. Cermak, S. C. Wasserman, and S. R. Manalis, "High-speed multiple-mode mass-sensing resolves dynamic nanoscale mass distributions," *Nature Commun.*, vol. 6, no. 1, p. 7070, May 2015.
- [49] Y. T. Yang, C. Callegari, X. L. Feng, K. L. Ekinci, and M. L. Roukes, "Zeptogram-scale nanomechanical mass sensing," *Nano Lett.*, vol. 6, no. 4, pp. 583–586, Apr. 2006.
- [50] M. S. Hanay et al., "Single-protein nanomechanical mass spectrometry in real time," *Nature Nanotechnol.*, vol. 7, no. 9, pp. 602–608, Sep. 2012.
- [51] M. Li, H. X. Tang, and M. L. Roukes, "Ultra-sensitive NEMS-based cantilevers for sensing, scanned probe and very high-frequency applications," *Nature Nanotechnol.*, vol. 2, no. 2, pp. 114–120, Feb. 2007.
- [52] L. Comenencia Ortiz et al., "Low-power dual mode MEMS resonators with PPB stability over temperature," *J. Microelectromech. Syst.*, vol. 29, no. 2, pp. 190–201, Apr. 2020.
- [53] F. J. Giessibl, "Advances in atomic force microscopy," *Rev. Mod. Phys.*, vol. 75, no. 749, pp. 1–10, Jul. 2003.



**Wen Sui** (Graduate Student Member, IEEE) received the B.S. and M.S. degrees in mechanical engineering from Northeastern University, Shenyang, China, in 2016 and 2019, respectively. He is currently pursuing the Ph.D. degree with the Department of Electrical and Computer Engineering, University of Florida, Gainesville, FL, USA.

His current interests include wide bandgap semiconductor nano/microelectromechanical systems (MEMS)/nanoelectromechanical systems (NEMS) for harsh environment applications, such as gallium nitride (GaN), aluminum scandium nitride (AlScN), and silicon carbide (SiC) MEMS for applications in high-temperature and radiative environment.

Mr. Sui was a recipient of the Margaret A. Ross Fellowship from ECE, University of Florida, and the Finish Line Award from the Graduate School, University of Florida.



**Tahmid Kaisar** (Graduate Student Member, IEEE) received the B.S. degree in electrical and electronic engineering from the Bangladesh University of Engineering and Technology (BUET), Dhaka, Bangladesh, in 2018. He is currently pursuing the Ph.D. degree with the Department of Electrical and Computer Engineering (ECE), University of Florida, Gainesville, FL, USA.

His research interests include CMOS-microelectromechanical systems (MEMS) oscillator-based computing, MEMS/nanoelectromechanical systems (NEMS) oscillator for real-time sensing and timing applications, and nonlinear dynamics of 2-D material NEMS-based devices.

Mr. Kaisar was a recipient of the Best Research Work Award at the AVS 2021 International Symposium.



**Haoran Wang** received the B.S. degree in measuring and control technology and instruments from Tianjin University, Tianjin, China, in 2017, and the Ph.D. degree in electrical and computer engineering from the University of Florida, Gainesville, FL, USA, in 2021.

He is currently a Senior Scientist with Applied Materials Inc., Sunnyvale, CA, USA. His research interests include microelectromechanical systems (MEMS), optical MEMS, micro/nanofabrication, and piezoelectric transducers.



**Huikai Xie** (Fellow, IEEE) received the B.S. degree in microelectronics from the Beijing Institute of Technology, Beijing, China, in 1989, the M.S. degree in photonics from Tufts University, Medford, MA, USA, in 1998, and the Ph.D. degree in electrical and computer engineering from Carnegie Mellon University, Pittsburgh, PA, USA, in 2002.

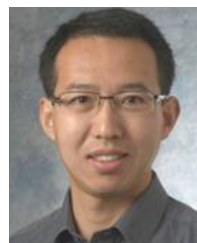
He was with the University of Florida, Gainesville, FL, USA, as an Assistant Professor, from 2002 to 2007; as a Tenured Associate Professor from 2007 to 2011; and as a full Professor from 2011 to 2020. He is currently a Professor with the School of Information and Electronics, Beijing Institute of Technology. He has authored or coauthored over 300 technical articles, 11 book chapters, and holds over 30 U.S. patents. His current research interests include microelectromechanical systems (MEMS)/nanoelectromechanical systems (NEMS), optical beam steering, optical communications, light detection and ranging (LiDAR), near infrared response (NIR) spectroscopy, and optical microendoscopy.

Dr. Xie is a Fellow of SPIE. He is also an Associate Editor of the IEEE SENSORS LETTERS and *Sensors and Actuators A: Physical*.



**Yihao Wu** (Graduate Student Member, IEEE) received the B.S. degree in electronics science and technology from the Beijing University of Technology (BJUT), Beijing, China, in 2021. He is currently pursuing the M.S. degree with the Department of Electrical and Computer Engineering (ECE), University of Florida, Gainesville, FL, USA.

His research interests include high-speed low-power data converter design, such as analog-to-digital converter, time-to-digital converter, and CMOS oscillator-based quantum-inspired computing.



**Philip X.-L. Feng** (Senior Member, IEEE) received the Ph.D. degree in electrical engineering (EE) from the California Institute of Technology (Caltech), Pasadena, CA, USA, in 2007.

He is currently a Professor with the Department of Electrical and Computer Engineering, University of Florida, Gainesville, FL, USA. He has mentored or co-mentored 13 Ph.D. students to the successful dissertation defense, mentored eight postdoctoral scholars, and also supervised 15 M.S. students with theses or research projects. His research is primarily focused on emerging solid-state devices and systems, particularly nano/microelectromechanical systems (NEMS/MEMS), atomic layer semiconductors and 2-D devices, silicon carbide (SiC) and other advanced semiconductors, quantum devices based on SiC and 2-D materials, as well as their integration with state-of-the-art ICs and optical/photonics technologies.

Dr. Feng is an alumnus of the National Academy of Engineering (NAE) U.S. Frontier of Engineering (USFOE) Program and subsequently a recipient of the NAE Grainger Foundation Frontiers of Engineering (FOE) Award. His awards also include the Presidential Early Career Award for Scientists and Engineers (PECASE) and the National Science Foundation CAREER Award. He and his students have won the six Best Paper/Presentation Awards at IEEE and other international conferences. He has served on the Technical Program Committees (TPCs) for the IEEE International Electron Devices Meeting (IEDM), the IEEE International Conference on Micro Electro Mechanical Systems (MEMS), International Conference on Solid-State Sensors, Actuators and Microsystems (Transducers), the IEEE International Frequency Control Symposium (IFCS) and European Frequency and Time Forum (EFTF), IEEE SENSORS, IEEE Nano, and other international conferences and workshops. He served as a Track Chair for IEEE SENSORS from 2016 to 2017, and as the TPC Group 4 Chair for the IEEE IFCS 2018, IFCS-EFTF 2019, and IFCS-ISAF 2020. He has also served as the Technical Program Chair for the MEMS/NEMS Technical Group at the 61st–63rd American Vacuum Society (AVS) International Symposium and Exhibition. He is also a Co-Organizer and the Technical Chair of the SiC Materials and Devices Workshop (since 2017). He has served as the Chair for the 34th IEEE International Conference on MEMS (IEEE MEMS 2021).



**Jaesung Lee** (Member, IEEE) received the B.S. and M.S. degrees in electrical engineering from the University of Electro-Communications (UEC), Tokyo, Japan, in 2007 and 2009, respectively, and the Ph.D. degree in electrical engineering from Case Western Reserve University (CWRU), Cleveland, OH, USA, in 2017.

He is currently an Assistant Professor with the Department of Electrical and Computer Engineering, University of Central Florida, Orlando, FL, USA. His research interests include developing functional nanodevices [e.g., nanoelectromechanical systems (NEMS)/microelectromechanical systems (MEMS), optoelectronic, and phononic devices] using advanced materials (e.g., 2-D crystals and wide bandgap semiconductors), toward building integrated systems for signal processing and sensing, in both classical and quantum regimes.

Dr. Lee is a Co-Technical Program Chair of the MEMS/NEMS Technical Group at the 69th American Vacuum Society (AVS) International Symposium and Exhibition.